Differential UWB Communications With Digital Multicarrier Modulation

Huilin Xu and Liuqing Yang, *Senior Member, IEEE*

***Abstract*—As a high-rate alternative of impulse radio (IR) ultrawideband (UWB) communications, analog and digital multicarrier UWB radios with coherent detection have been introduced. In this paper, we investigate digital multicarrier differential (MCD) modulation and demodulation schemes for UWB communications. In our approach, the differential encoding and decoding are carried out across multiple digital carriers in the frequency domain. Hence, channel estimation is bypassed by using neighboring carriers as reference carriers. Compared with the transmitted reference TR-UWB which relies on delaying and correlating the received signal segments in time domain, our MCD-UWB avoids the need for analog delay elements. In addition, our digital-carrier based approach does not incur any spectrum expansion. We also show that our approach enables variable data rates, and remains operational even in the presence of severe interframe interference (IFI). In addition, the small spacing between differentially encoded carriers ensures that the data rate is not limited by the channel coherence bandwidth. Furthermore, our schemes are flexible in providing variable-rate transmissions. Simulations are also carried out to corroborate our theoretical analysis.**

***Index Terms*—Differential modulation and demodulation, digital multicarrier, ultrawideband (UWB).**

I. Introduction

SINCE the release of the ultrawideband (UWB) spectral mask by the Federal Communications Commission, there has been an increasing interest in UWB communications. Due to its fine multipath resolution and carrier-free operation, UWB becomes a promising candidate for short-range high-speed wireless communications in dense multipath environments [19], [21]. To collect the ample multipath diversity, RAKE reception is often referred to as the optimal coherent detector, provided that the channel information is available at the receiver. However, the extremely rich multipath of the UWB channel poses challenges in channel estimation and, accordingly, in the realization of the RAKE receiver. To bypass the explicit channel estimation, semi-coherent approaches including the transmitted-reference (TR) (see, e.g., [1], [4], [10], [14]) and differential (see, e.g., [7]–[9]) systems as well as noncoherent techniques [22] have been proposed. These approaches result in simple transceiver structures. However, the required ultrawideband analog delay element may be difficult to implement at the IC level.

To amend this problem, frequency-shifted reference (FSR) UWB was recently proposed [6], where the reference and information-conveying signals are transmitted simultaneously on two orthogonal frequency tones. Unlike TR-UWB and existing semi/noncoherent approaches, FSR-UWB does not need the analog delay line. However, similar to TR-UWB which uses half of the total energy on the reference pulses, FSR-UWB induces the energy loss by allocating equal energies on the information-conveying tone and the reference tone. In [23], a multidifferential (MD) FSR-UWB scheme was proposed to improve the data rate of the original FSR-UWB by using a single reference tone together with multiple data tones. However, this approach requires that all carriers locate within the channel coherence bandwidth. This constraint restricts the number of usable carriers and thereby limits the overall data rate. Although FSR-UWB has been shown to be robust to the interframe interference in simulations, it was developed under the assumption that the interframe interference (IFI) and intersymbol interference (ISI) are negligible [5], [6]. This can limit the data rate of the UWB system. Moreover, MD-FSR-UWB modulates the transmitted UWB pulses with analog carriers, which induce bandwidth expansion and can give rise to frequency offset by having mismatched oscillators at the transmitter and receiver.

To address these limitations, we introduce in this paper digital multicarrier differential (MCD) signaling schemes for UWB systems. Different from exiting multicarrier UWB techniques that use coherent detectors [2], [16], [20], our MCD-UWB bypasses the channel estimation via frequency-domain differential (de-)modulation. Inspired by the FSR-UWB schemes, our MCD-UWB avoids the analog delay line. However, our approach outperforms the FSR-UWB by considerably reducing energy loss, and the bandwidth expansion induced by the analog-carrier modulation. Equally attractive is that our MCD-UWB allows for high and variable data rates without increasing the spacing among the reference and data tones. This is to be contrasted with the MD-FSR-UWB where the average spacing between data and reference tones increases with the data rate. By allowing for (possibly severe) IFI and ISI, the data rates of MCD-UWB can be further boosted. Our MCD-UWB systems can be implemented with fast Fourier transform (FFT) and discrete cosine transform (DCT) circuits. It is worth stressing that all these digital processing deals with the discrete time signal sampled at the *frame-rate*, as opposed to the pulse-rate or Nyquist-rate which can be easily several gigahertz. Finally, we will also prove that our MCD-UWB can effectively collect the multipath diversity even in the presence of IFI.

Manuscript received September 5, 2006; revised April 17, 2007. The associate editor coordinating the review of this paper and approving it for publication was Dr. Kostas Berberidis. This work was supported by the National Science Foundation under Grant ECS-0621879. Parts of the results in this paper have been accepted by the IEEE International Conference on Ultra Wideband 2006 and the IEEE Globecom 2006.

The authors are with the Department of Electrical and Computer Engineering, University of Florida, Gainesville, FL 32611 USA (e-mail: xuhl@ufl.edu; lqyang@ece.ufl.edu).

Digital Object Identifier 10.1109/TSP.2007.901656

Notation: We will use bold upper (lower) case letters to denote matrices (column vectors) and $\boldsymbol{F}$ to denote the FFT matrix. We will use $(\cdot)^T$ and $(\cdot)^{\mathcal{H}}$ for transpose and conjugated transpose, $\mathrm{diag}\{\boldsymbol{a}\}$ for a diagonal matrix with $\boldsymbol{a}$ sitting on the diagonal, and $\delta_{m,n}$ for Kronecker delta.

II. Digital Multicarrier Transmission Model

In this section, we will introduce the transmitted signal model using multiple digital carriers. We will start from the real carriers and then generalize to the complex case.

A. Real Multicarrier Differential Modulation

Here, we adopt the $(N_f/2+1)$ column vectors $\boldsymbol{g}_n := [g_n(0),\ldots,g_n(N_f-1)]^T$, $n=0,1,\ldots,N_f/2$, as our digital carriers

$$g_n(k)=\begin{cases}\sqrt{\frac{2}{N_f+2}}\cos(2\pi f_n k), & n=0, or, n=\frac{N_f}{2}\\ \sqrt{\frac{4}{N_f+2}}\cos(2\pi f_n k), & n\in[1,\frac{N_f}{2}-1]\end{cases} \quad (1)$$

where N_f is the number of frames transmitted during each block period and $f_n := n/N_f$.

These real digital carriers are reminiscent of those introduced in [20] to facilitate multiple access in UWB systems. However, instead of the N_f carriers in [20], we have only $(N_f/2+1)$ in (1); that is, the $(N_f/2-1)$ sin-based carriers in [20] are dropped here. Intuitively, the sin- and cos-based digital carriers share the same frequency tones with differing polarity. In [20], coherent detection is used to separate these carriers. However, due to the phase ambiguity inherent to differential detectors, the sin and cos carriers become indistinguishable. Hence, we only adopt the $(N_f/2+1)$ cosine waveforms. Stacking the $(N_f/2+1)$ vectors into a matrix, we have $\boldsymbol{G} := [\boldsymbol{g}_0,\ldots,\boldsymbol{g}_{N_f/2}]$. Evidently, it follows that $\boldsymbol{G}^T\boldsymbol{G}=2N_f/(N_f+2)\boldsymbol{I}_{N_f/2+1}$ by construction.

Consider a block-by-block transmission where, during the kth block, the real digital carriers are modulated by $(N_f/2+1)$ real symbols $\boldsymbol{d}_k^R := \left[d_k^R(0),\ldots,d_k^R(N_f/2)\right]^T$, with $\boldsymbol{d}_k^R$ satisfying $E\left\{d_k^R(n)d_k^R(m)\right\}=\delta_{m,n}$ and the superscript "R" indicating the "real" carrier case. The resultant N_f signals collected by $\boldsymbol{a}_k^R := \left[a_k^R(0),\ldots,a_k^R(N_f-1)\right]^T$ is obtained as $\boldsymbol{a}_k^R=\boldsymbol{G}\boldsymbol{d}_k^R$. Adopting the widely-accepted notation in the UWB literature, we let each $a_k^R(n)$, $n\in[0,N_f-1]$, be transmitted over one frame of duration T_f. Accordingly, each block consists of N_f such frames, and has a duration $T_s=N_fT_f$. Using the ultrashort UWB pulse shaper $p(t)$, we obtain the following transmitted signal model:

$$x^R(t)=\sqrt{\mathcal{E}_p}\sum_{k=0}^{\infty}\sum_{n=0}^{N_f-1}a_k^R(n)p(t-kT_s-nT_f) \quad (2)$$

where $\mathcal{E}_p$ is the energy per pulse. In the ensuing sections, we will discuss how $d_k^R(n)$'s are generated using differential encoding to facilitate variable data rates and how they are differentially demodulated.

B. Complex Multicarrier Differential Modulation

As we discussed before, the maximum number of real carriers is $(N_f/2+1)$. Later, we will see that this also dictates the maximum number of distinct symbols transmitted per block. To increase the number of digital carriers, one can resort to the set of N_f complex carriers $\{\boldsymbol{f}_n\}_{n=0}^{N_f-1}$ which are simply the columns of the $N_f\times N_f$ FFT matrix $\boldsymbol{F}^{\mathcal{H}}$. During the kth block, these digital carriers are modulated by N_f complex symbols $\boldsymbol{d}_k^C := \left[d_k^C(0),\ldots,d_k^C(N_f-1)\right]^T$ to generate N_f signals collected by $\boldsymbol{a}_k^C := \boldsymbol{a}_k^r+\jmath\boldsymbol{a}_k^i=\boldsymbol{F}^{\mathcal{H}}\boldsymbol{d}_k^C=\left[a_k^C(0),\ldots,a_k^C(N_f-1)\right]^T$, where the superscript "C" indicates the "complex" carrier case. Notice that $\boldsymbol{a}_k^C$ is generally complex. This implies that the carrierless signal model (2) is not directly applicable. But even without an analog carrier, the real and imaginary parts of the vector $\boldsymbol{a}_k^C$ can be transmitted over two consecutive blocks each of duration T_s

$$x^C(t)=\sqrt{\mathcal{E}_p}\sum_{k=0}^{\infty}\sum_{n=0}^{N_f-1}a_k^r(n)p(t-2kT_s-nT_f) +\sqrt{\mathcal{E}_p}\sum_{k=0}^{\infty}\sum_{n=0}^{N_f-1}a_k^i(n)p(t-(2k+1)T_s-nT_f). \quad (3)$$

Notice that each of the two summands in (3) is essentially the same as (2). Unlike the real MCD that only requires frame-level synchronization, the complex case also entails symbol-level synchronization to locate the starting point of each real-imaginary pair. Using these transmitted signal models, we will next introduce the channel propagation effects and the received signal models.

III. Channel Effects and Received Signal Model

In the preceding section, we have seen that $\boldsymbol{a}_k^R$, $\boldsymbol{a}_k^r$, and $\boldsymbol{a}_k^i$ share the same transmitted signal model. Therefore, when deriving the received signal in this section we will first consider the generic transmitted block $\boldsymbol{a}_k := [a_k(0),\ldots,a_k(N_f-1)]^T$, and then specify the model for the real and complex cases towards the end of this section. The transmitted signal $x(t)=\sqrt{\mathcal{E}_p}\sum_{k=0}^{\infty}\sum_{n=0}^{N_f-1}a_k(n)p(t-kT_s-nT_f)$ [cf. (2) and (3)] propagates through the multipath channel with impulse response $\sum_{l=0}^{L-1}\beta(l)\delta(t-\tau(l))$, where $\{\beta(l)\}_{l=0}^{l=L-1}$ and $\{\tau(l)\}_{l=0}^{l=L-1}$ are amplitudes and delays of the L multipath elements, respectively. Then, the received waveform is given by

$$r(t)=\sqrt{\mathcal{E}_p}\sum_{k=0}^{\infty}\sum_{n=0}^{N_f-1}a_k(n)h(t-kT_s-nT_f)+\eta(t) \quad (4)$$

where $h(t)=\sum_{l=0}^{L-1}\beta(l)p(t-\tau(l))$ is the composite pulse waveform after the multipath propagation and $\eta(t)$ is the additive white Gaussian noise. We assume $\tau(0)=0$, which means perfect timing synchronization is achieved at the receiver. It is worth noting that we are not imposing any constraint on the frame duration T_f. In other words, to facilitate high data rates, the frame duration is allowed to be less than the channel delay

spread ($T_f < \tau(L-1)+T_p$). Notice that in such cases, IFI and ISI emerge.

At the receiver, a bank of L_c correlators are used to collect the multipath energy. Each correlator uses a single delayed pulse $p(t)$ as the template and the correlator output is sampled at the *frame-rate*. This can be interpreted as the parallel counterpart of the single correlator with a T_s-long template in FSR-UWB. Let $\{\tau_c(l)\}_{l=1}^{L_c}$ ($\tau_c(l) < \tau_c(l+1)$, $\forall\, l \in [1, L_c-1]$) denote the delays associated with the L_c correlators. As the correlation is carried out on a per frame basis, the correlator delays are upper bounded by the frame duration T_f. In addition, they should not exceed the channel delay spread to ensure effective energy collection. Hence, we have $\tau_c(L_c) \leq \max\{\tau(L-1),\, T_f - T_p\}$.

During the nth frame of the kth block, the template for the lth correlator is the pulse $p(t - kT_s - nT_f - \tau_c(l))$, and the correlator output is $y_k(l;n) := \int_{kT_s+nT_f}^{kT_s+nT_f+T_f} r(t)p(t - kT_s - nT_f - \tau_c(l))dt$. Denoting the correlation between the template and the received composite impulse waveform $h(t)$ as $\beta_c(l;m) := \int_{mT_f}^{mT_f+T_f} h(t)p(t - mT_f - \tau_c(l))dt = \sum_{l'=0}^{L-1} \beta(l')R_p(\tau(l') - mT_f - \tau_c(l))$, where $R_p(\tau) := \int_0^{T_f} p(t)p(t-\tau)dt$ is the auto-correlation function of $p(t)$, we can re-express the frame-rate samples of the lth correlator as

$$y_k(l;n) = \sqrt{\mathcal{E}_p}\sum_{m=0}^{n}\beta_c(l;m)a_k(n-m) + \sqrt{\mathcal{E}_p}\sum_{m=n+1}^{M_l}\beta_c(l;m)a_{k-1}(N_f - m + n) + \eta_k(l;n) \quad (5)$$

where $\eta_k(l;n)$ is the noise sample at the correlator output. From (5), it follows that $\{\beta_c(l;m)\}_{m=0}^{M_l}$ can be regarded as the discrete-time equivalent impulse response of the channel. The order of this channel can be determined as $M_l := \max\{m : \tau_c(l) + mT_f < \tau(L_c) + T_p\}$. Notice that, as long as $M_l > 0$, for any $l \in [1, \ldots, L_c]$, IFI and ISI are both present. Hereafter, we will let $M_h := \max_l\{M_l\}$ denote the maximum order of the discrete-time equivalent channel.

Stacking the outputs corresponding to the kth block from the lth correlator to form the vector $\boldsymbol{y}_k(l) := [y_k(l;0), \ldots, y_k(l;N_f-1)]^T$, we obtain the input–output (I/O) relationship in a matrix-vector form

$$\boldsymbol{y}_k(l) = \sqrt{\mathcal{E}_p}\boldsymbol{H}_l^{(0)}\boldsymbol{a}_k + \sqrt{\mathcal{E}_p}\boldsymbol{H}_l^{(1)}\boldsymbol{a}_{k-1} + \boldsymbol{\eta}_k(l) \quad (6)$$

where $\boldsymbol{\eta}_k(l)$ is the noise vector, $\boldsymbol{H}_l^{(0)}$ is an $N_f \times N_f$ lower triangular Toeplitz matrix with the first column being $[\beta_c(l;0), \ldots, \beta_c(l;M_l), 0, \ldots, 0]^T$, and $\boldsymbol{H}_l^{(1)}$ is an $N_f \times N_f$ upper triangular Toeplitz matrix with the first row being $[0, \ldots, 0, \beta_c(l;M_l), \ldots, \beta_c(l;1)]$. Due to the multipath channel effect, $\boldsymbol{y}_k(l)$ depends on both $\boldsymbol{a}_k$ and $\boldsymbol{a}_{k-1}$. The IFI and ISI we mentioned before now take the form of interblock interference (IBI).

To facilitate block-by-block detection, one could use either the cyclic prefix (CP) or padding zeros (ZP) to remove IBI [17]. With the CP option, IBI can be eliminated by inserting a CP of length M_h at the transmitter and discarding it at the receiver. Correspondingly, the system I/O relationship is given by

$$\tilde{\boldsymbol{y}}_k(l) = \sqrt{\mathcal{E}_p}\tilde{\boldsymbol{H}}_l\boldsymbol{a}_k + \tilde{\boldsymbol{\eta}}_k(l) \quad (7)$$

where the channel matrix $\tilde{\boldsymbol{H}}_l$ becomes a column-wise circulant matrix with the first column being $[\beta_c(l;0), \ldots, \beta_c(l;M_l), 0, \ldots, 0]^T$.

Now, we are ready to specify the received signals for the real and complex carriers. For the real carriers, the received signal on the lth correlator after CP removal is simply $\boldsymbol{y}_k^R(l) = \tilde{\boldsymbol{y}}_k(l)$. For the complex carriers, the received block consists of two combined ones: $\boldsymbol{y}_k^C(l) = \tilde{\boldsymbol{y}}_{2k}(l) + j\tilde{\boldsymbol{y}}_{2k+1}(l)$. From (7), it follows that their respective I/O relationships are

$$\begin{aligned}\boldsymbol{y}_k^R(l) &= \sqrt{\mathcal{E}_p}\tilde{\boldsymbol{H}}_l\boldsymbol{a}_k^R + \boldsymbol{\eta}_k^R(l)\\ \boldsymbol{y}_k^C(l) &= \sqrt{\mathcal{E}_p}\tilde{\boldsymbol{H}}_l\boldsymbol{a}_k^C + \boldsymbol{\eta}_k^C(l)\end{aligned} \quad (8)$$

where $\boldsymbol{\eta}_k^R(l)$ and $\boldsymbol{\eta}_k^C(l)$ are the real and complex frame-rate noise samples, respectively. As IBI is eliminated, we will drop the block index k hereafter.

The $N_f \times N_f$ circulant matrix $\tilde{\boldsymbol{H}}_l$ can be diagonalized by pre- and post-multiplication with the N_f-point FFT and IFFT matrices; that is, $\boldsymbol{F}\tilde{\boldsymbol{H}}_l\boldsymbol{F}^{\mathcal{H}} = \boldsymbol{D}_H := \mathrm{diag}\{H_l(0), \ldots, H_l(N_f-1)\}$, where $H_l(n) = \sum_{m=0}^{M_l}\beta_c(l;m)\exp(-j2\pi nm/N_f)$ is the frequency response of the equivalent channel. The measurement results of UWB channels in [3] and [11] show that the root-mean-square (rms) delay spread σ_{rms} is at the level of 5 ns. Accordingly, the coherence bandwidth is about $1/(5\sigma_{\mathrm{rms}}) \approx 40$ MHz [13]. Considering a UWB system with $N_f = 32$ and $T_f = 24$ ns, with which our simulations are carried out, the carrier spacing $1/(N_fT_f) \approx 1.3$ MHz is much smaller than the channel coherence bandwidth. Therefore, it holds that $H_l(n) \approx H_l(n+1), n \in [0, \ldots, N_f-2]$. In other words, the channel for adjacent carriers are approximately identical.

Denoting the complex multicarrier demodulation results of the frame-rate sampled output for the lth correlator by $\boldsymbol{v}^C(l) := \boldsymbol{F}\boldsymbol{y}^C(l) = \left[v^C(l;0), \ldots, v^C(l;N_f-1)\right]^T$ and applying FFT on both sides of (7), we obtain the system I/O relationship as

$$\boldsymbol{v}^C(l) = \boldsymbol{F}\boldsymbol{y}^C(l) = \sqrt{\mathcal{E}_p}\boldsymbol{D}_H(l)\boldsymbol{d}^C + \boldsymbol{\zeta}^C(l) \quad (9)$$

where $\boldsymbol{\zeta}^C(l)$ is the noise vector.

For the case of real carriers, it can be easily proved that $\boldsymbol{G}^T\tilde{\boldsymbol{H}}_l\boldsymbol{G}$ is an $(N_f/2+1) \times (N_f/2+1)$ diagonal matrix with the diagonal entries given by

$$2N_f\sqrt{N_f}/(N_f+2)\Re\left\{\boldsymbol{F}_{1:N_f/2+1}^{\mathcal{H}}\right\}\boldsymbol{\beta}_c(l) = 2N_f/(N_f+2)\Re\{\boldsymbol{D}_H(l)\}$$

where $\boldsymbol{\beta}_c(l) = [\beta_c(l;0), \ldots, \beta_c(l;M_l), 0, \ldots, 0]^T$.

Defining the real multicarrier demodulation results of the frame-rate sampled output for the lth correlator by

$\boldsymbol{v}^R(l) := \boldsymbol{G}^T\boldsymbol{y}^R(l)$, we obtain the equivalent system I/O relationship as

$$\boldsymbol{v}^R(l)=\boldsymbol{G}^T\boldsymbol{y}^R(l)=\frac{2N_f}{N_f+2}\sqrt{\mathcal{E}_p}\Re\{\boldsymbol{D}_H(l)\}\boldsymbol{d}^R+\boldsymbol{\zeta}^R(l) \quad (10)$$

where $\boldsymbol{\zeta}^R(l)$ is the noise vector.

Using the I/O models (9) and (10), we will next introduce the construction of $\boldsymbol{d}^C$ and $\boldsymbol{d}^R$ (the differential encoding) at the transmitter and the restoration of the information (the differential decoding) at the receiver.

IV. Differential Demodulation With Variable Data Rates

In the preceding sections, we have established the I/O relationships for real and complex multicarrier UWB systems. With typical UWB system parameters, the equivalent channel coefficients, $H_l(n)$ for complex carriers and $\Re\{H_l(n)\}$ for real carriers, vary slowly across n in the frequency domain. This allows for differential (de-)modulation across neighboring carriers.

This idea is reminiscent of the FSR-UWB [6]. However, our design will turn out to facilitate variable data rates, without any bandwidth expansion and with considerably improved energy efficiency. More importantly, under certain circumstances, no reference tone is needed. This translates to *zero* energy loss.

Since FFT-based complex multicarrier communication is better understood, we will present the differential demodulation for the complex carriers followed by that for the real carriers at different data rate levels.

A. High-Rate MCD-UWB

1) Complex Carriers: In the high-rate implementation, the entries of vector $\boldsymbol{d}^C$ are differentially encoded as follows:

$$d^C(n)=\begin{cases}1, & n=0\\ d^C(n-1)s(n-1), & n\in[1,\ldots,N_f-1]\end{cases} \quad (11)$$

where $\{s(n)\}_{n=0}^{N_f-2}$ are the M-ary phase-shift keying (PSK) information symbols. As a result, only the first carrier is used as an unmodulated reference, while the rest (N_f-1) carriers each conveys a distinct information symbol. Notice that, though the usage of an unmodulated reference carrier is reminiscent of the FSR-UWB, our digital carriers facilitate considerably higher rate with no bandwidth expansion. Furthermore, in typical UWB systems with large N_f, the cost of the reference carrier can be neglected and the bandwidth and energy efficiencies approach 100% as N_f increases.

Based on (11), and using the approximation that $H(n)\approx H(n+1)$, $\forall\, n\in[0,\ldots,N_f-2]$, differential decoding can be performed on the FFT of the *frame-rate* samples $\boldsymbol{v}^C(l)$ to recover the transmitted symbols without attempting to estimate the channel. Specifically, in the absence of noise, we have

$$\begin{aligned}v^C(l;n+1)(v^C(l;n))^* &=\mathcal{E}_pH_l(n+1)H_l^*(n)d(n+1)d^*(n)\\ &\approx\mathcal{E}_p|H_l(n)|^2s(n).\end{aligned} \quad (12)$$

To establish a more convenient representation, we define the following $N_f\times N_f$ circularly shifting matrix

$$\boldsymbol{J}=\begin{bmatrix}0 & 1 & 0 & \ldots & 0\\ & & \ddots & \ddots & \vdots\\ \vdots & & \ddots & 1 & 0\\ 0 & & \ldots & 0 & 1\\ 1 & 0 & \ldots & & 0\end{bmatrix} \quad (13)$$

and formulate the $N_f\times N_f$ matrix

$$\boldsymbol{U}^C=\sum_{l=1}^{L_c}\boldsymbol{v}^C(l)(\boldsymbol{v}^C(l))^{\mathcal{H}}\boldsymbol{J} \quad (14)$$

where, to effectively collect energy, we sum up the differential decoding results from all correlators. Clearly, the decision statistics for $[s(0),\ldots,s(N_f-2)]^T$ are the last (N_f-1) diagonal entries of $\boldsymbol{U}^C$; that is

$$u_H^C(n)=[\boldsymbol{U}^C]_{n,n}\approx\mathcal{E}_p\sum_{l=1}^{L_c}|H_l(n-1)|^2s(n-1)+\xi_H^C(n),\quad n\in[1,\ldots,N_f-1] \quad (15)$$

where $\xi_H^C(n)$ is the noise term and the "$\approx$" comes from the approximation $H_l(n)\approx H_l(n+1), n\in[0,\ldots,N_f-2]$ in UWB channels.

The receiver structure is illustrated in Fig. 1. After passing through a bank of L_c correlators, the received signal $r(t)$ is sampled at the frame-rate to generate the discrete-time signal $\{\boldsymbol{y}^C(l)\}_{l=1}^{L_c}$. With the multicarrier demodulation by multiplying $\boldsymbol{F}$ and the differential decoding for each correlator branch l, the resultant signals are summed up across all correlators to obtain the decision statistics for the transmitted information symbols.

2) Real Carriers: For the case of real carriers, the entries of $\boldsymbol{d}^R$ are differentially constructed as follows:

$$d^R(n)=\begin{cases}1, & n=0\\ d^R(n-1)b(n-1), & n\in\left[1,\ldots,\frac{N_f}{2}\right]\end{cases} \quad (16)$$

where the information bits $\{b(n)\}_{n=0}^{N_f/2}$ are BPSK modulated. Similar to the complex carriers, only the first carrier is used as the unmodulated reference, and each of the rest $N_f/2$ carriers conveys a distinct information bit. Similar to (12), we have $v^R(l;n+1)v^R(l;n)\approx 4\mathcal{E}_pN_f^2/(N_f+2)^2\Re\{H_l(n)\}^2b(n)$. Then, differential decoding can be performed on $\boldsymbol{v}^R(l)$ for each correlator branch l. Let $\boldsymbol{J}^R$ denote the $(N_f/2+1)\times(N_f/2+1)$ circularly shifting matrix, which has the same structure as $\boldsymbol{J}$ in (13) but with a smaller dimension. We can then formulate the following $(N_f/2+1)\times(N_f/2+1)$ matrix

$$\boldsymbol{U}^R=\sum_{l=1}^{L_c}\boldsymbol{v}^R(l)(\boldsymbol{v}^R(l))^T\boldsymbol{J}^R. \quad (17)$$

As in (14), we sum up the differential demodulation results from all correlators to effectively collect the channel energy. Then,

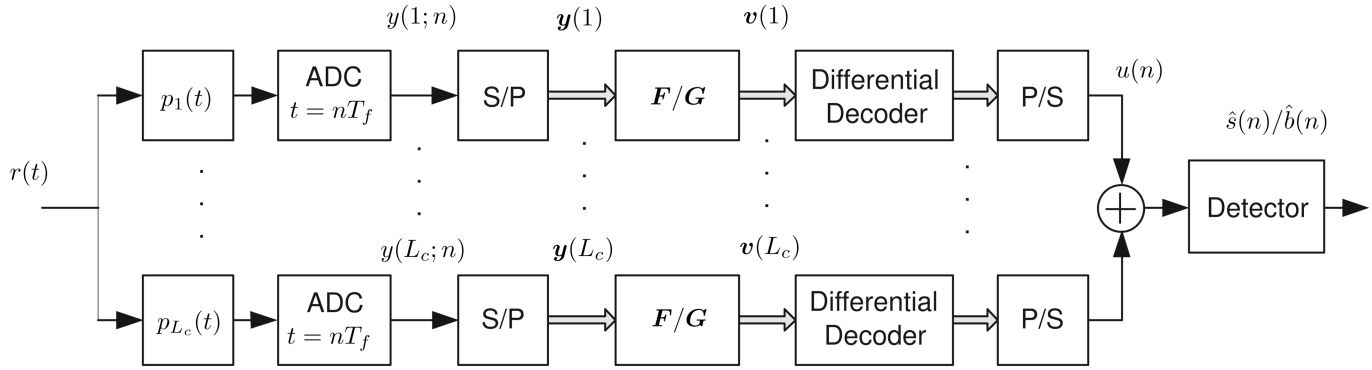

Fig. 1. Receiver diagram for high-rate MCD-UWB, where we use $p_l(t)$ to denote $p(t-\tau_c(l))$ and omit all superscripts for notational brevity.

the decision statistics for $[b(0),\ldots,b(N_f/2-1)]^T$ are the last $N_f/2$ diagonal entries of $\boldsymbol{U}^R$

$$u_H^R = [\boldsymbol{U}^R]_{n,n} \approx \frac{4\mathcal{E}_p N_f^2}{(N_f+2)^2}\sum_{l=1}^{L_c}\Re\{H_l(n-1)\}^2 \cdot b(n-1) + \xi_H^R(n), \quad n \in \left[1,\ldots,\frac{N_f}{2}\right] \tag{18}$$

where $\xi_H^R(n)$ is the noise term and the "$\approx$" comes from the approximation $\Re\{H_l(n)\} \approx \Re\{H_l(n+1)\}$.

For the case of real carriers, the receiver structure is similar to that for the complex carriers (see Fig. 1), except that the multicarrier demodulation is performed by multiplying $\boldsymbol{G}$. Again, the decoding results are summed up across all correlators to obtain the decision statistics for the transmitted information symbols.

Remark 1: The MD-FSR-UWB [23] scheme can also enable a higher data rate than the original FSR-UWB [6] by using a single reference tone together with multiple data tones. However, this approach requires that all carriers remain within the channel coherence bandwidth. This constraint restricts the number of usable carriers and, therefore, limits the data rate. Our high-rate MCD-UWB techniques relax the constraint by only requiring $H_l(n) \approx H_l(n+1)$, $n \in [0,\ldots,N_f-2]$, and, therefore, can use all carriers to enable the maximum data rate. Furthermore, the development of MD-FSR-UWB in [23] assumes that IFI is absent by choosing a T_f that is sufficiently long. This also limits the data rate. In MCD-UWB we develop here, severe IFI is allowed to enable high-rate transmission. In addition, higher data rate in MD-FSR-UWB comes at the price of having more analog carriers. This implies a larger bandwidth expansion. To be specific, when N data tones are used with MD-FSR-UWB scheme, the bandwidth expansion is $2N/T_s$. On the contrary, our MCD-UWB relies on digital carriers that do not induce any bandwidth expansion.

B. Low-Rate MCD-UWB

Letting $s(n) = s, \forall\, n \in [0, N_f-2]$, in (11), and $b(n) = b$, $\forall\, n \in [0, N_f/2-1]$, in (16), we obtain the low-rate version of our multicarrier differential scheme. The resultant data rate $1/T_s$ symbols/s turns out to be the same as the FSR-UWB in [6]. However, we will show, both analytically and by simulations, that with more carriers conveying the same information, our low-rate schemes can capture the multipath diversity, and can considerably reduce the energy loss encountered by FSR-UWB. More importantly, under certain conditions, no reference carriers are needed and the energy loss can be completely avoided.

1) Complex Carriers: When all carriers carry the same information symbol s, (11) becomes

$$d^C(n) = \begin{cases} 1, & n = 0 \\ d^C(n-1)s, & n \in [1,\ldots,N_f-1] \end{cases} \tag{19}$$

where s is the M-ary PSK information symbol. Since (19) is a special case of (11), the same demodulator (14) can be applied here. However, taking into account that the diagonal entries of $\boldsymbol{U}^C$ are the decision statistics for the same symbol s, we have

$$u_L^C = \sum_{n=1}^{N_f-1}[\boldsymbol{U}^C]_{n,n} = \sum_{l=1}^{L_c}(\boldsymbol{v}^C(l))^{\mathcal{H}}\boldsymbol{J}\boldsymbol{v}^C(l) \approx \mathcal{E}_p\sum_{n=1}^{N_f-1}\sum_{l=1}^{L_c}|H_l(n-1)|^2 s + \xi_L^C \tag{20}$$

where ξ_L^C is the noise term. Along the lines of [12, ch. 5], the variance of ξ_L^C can be shown to be $\sigma_\xi^2 = 2\mathcal{N}_0\mathcal{E}_p\sum_{l=1}^{L_c}\sum_{n=1}^{N_f-1}|H_l(n-1)|^2$, where $\mathcal{N}_0$ is the variance of the time-domain sampled complex noise at the correlator outputs.

Notice that, since one reference carrier is used, the energy of reference carrier of MCD-UWB can be neglected as N_f increases. This is to be contrasted with the FSR-UWB, where half of the energy is used by the reference carrier. In fact, the energy loss entailed by the reference carrier can be completely avoided. To see this, notice that when the *digital* carriers are employed we have also $H(0) \approx H(N_f-1)$, as a byproduct of the discrete-time FFT.

Hence, if the signals riding on the first and last carriers are also differentially related with respect to the information symbol s, that is, $d^C(0) = d^C(N_f-1)s$, then the noise-free product $v^C(l;0)(v^C(l;N_f-1))^*$ turns out to be

$$\mathcal{E}_p H_l(0)H_l^*(N_f-1)d^C(0)(d^C(N_f-1))^* \approx \mathcal{E}_p|H_l(N_f-1)|^2.$$

Recalling that $d^C(0) = 1$ [cf. (19)], we deduce that the symbol s has to satisfy $s^{N_f} = 1$. In other words, as long as

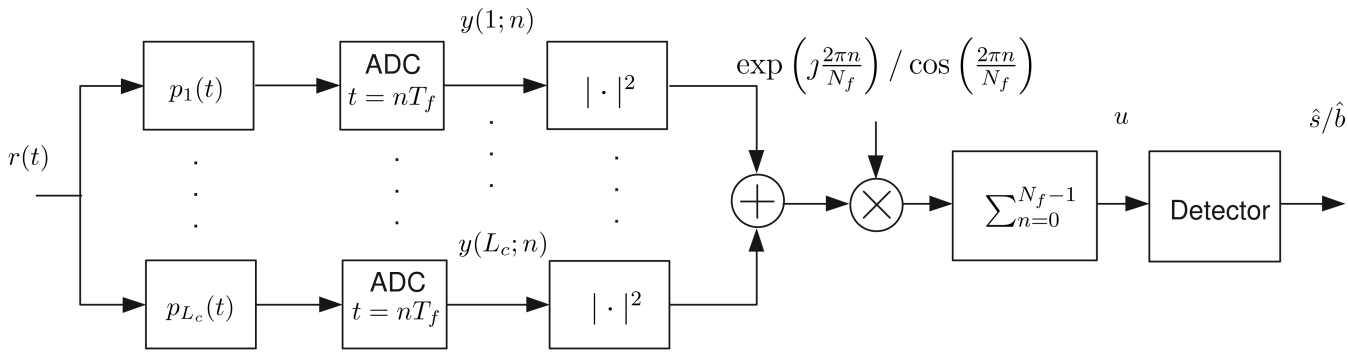

Fig. 2. Receiver diagram for low-rate MCD-UWB, where we use $p_l(t)$ to denote $p(t-\tau_c(l))$ and omit all superscripts for notational brevity.

the PSK modulation size M is an integer factor of N_f,[1] our differential decoding can be carried out between all adjacent pairs of digital carriers without any reference tone. In this case, the decision statistic can be alternatively expressed as

$$u_L^C = \sum_{n=0}^{N_f-1} [\boldsymbol{U}^C]_{n,n} = \sum_{l=1}^{L_c} (\boldsymbol{v}^C(l))^{\mathcal{H}} \boldsymbol{J} \boldsymbol{v}^C(l) \approx \mathcal{E}_p \sum_{l=1}^{L_c} \sum_{n=0}^{N_f-1} |H_l(n)|^2 s + \xi_L^C. \quad (21)$$

Notice that the summand limits in (21) are different from those in (20).

Interestingly, the decision statistic in (21) implies a simpler receiver implementation. As a circulant matrix, $\boldsymbol{J}$ can be diagonalized by pre- and post-multiplication with the FFT and IFFT matrices, i.e., $\boldsymbol{F}^{\mathcal{H}}\boldsymbol{J}\boldsymbol{F} = \boldsymbol{D}_J$, whose nth diagonal entry is $[\boldsymbol{D}_J]_{n,n} = \exp(j2\pi n/N_f)$. In other words, the diagonal of $\boldsymbol{D}_J$ is exactly the second column of $\sqrt{N_f}\boldsymbol{F}^{\mathcal{H}}$. Substituting $\boldsymbol{J} = \boldsymbol{F}\boldsymbol{D}_J\boldsymbol{F}^{\mathcal{H}}$ into (21), and recalling that $\boldsymbol{v}^C(l) = \boldsymbol{F}\boldsymbol{y}^C(l)$, one can re-express u_L^C as

$$u_L^C = \sum_{l=1}^{L_c} (\boldsymbol{y}^C(l))^{\mathcal{H}} \boldsymbol{D}_J \boldsymbol{y}^C(l) = \sum_{l=1}^{L_c} \sum_{n=0}^{N_f-1} |y^C(l;n)|^2 e^{\jmath(2\pi n/N_f)} + \xi_L^C. \quad (22)$$

Equation (22) reveals that the FFT operation at the receiver can be avoided.

The simplified receiver structure is illustrated in Fig. 2. It is essentially the digital version of the low-rate FSR-UWB receiver in [6]. It is worth stressing that this digital receiver operates on the *frame-rate* samples generated when the received signal $r(t)$ passes through the correlator bank. The differential decoding is then performed by correlating $\{|y^C(l;n)|^2\}_{n=0}^{N_f-1}$ with the complex carrier $\{\exp(j2\pi n/N_f)\}_{n=0}^{N_f-1}$ on each correlator branch l, and then summing them up across the L_c correlators.

[1]With typically large and even N_f, this condition is not very restrictive for practical modulation sizes.

2) Real Carriers: When all the real carriers carry the same information bit b, (16) becomes

$$d^R(n) = \begin{cases} 1, & n = 0 \\ d^R(n-1)b, & n \in \left[1, \ldots, \left(\frac{N_f}{2}\right)\right] \end{cases} \quad (23)$$

where the information bit b is a BPSK symbol. As (23) is a special case of (16), the same demodulator (17) can be applied here. However, taking into account that the diagonal entries of $\boldsymbol{U}^R$ are the decision statistics for the same symbol b, we have

$$u_L^R = \sum_{n=1}^{N_f/2} [\boldsymbol{U}^R]_{n,n} = \sum_{l=1}^{L_c} \sum_{n=1}^{N_f/2} v^R(l;n) v^R(l;n-1) \approx \frac{4\mathcal{E}_p N_f^2}{(N_f+2)^2} \sum_{l=1}^{L_c} \sum_{n=1}^{N_f/2} \Re\{H_l(n-1)\}^2 \cdot b + \xi_L^R \quad (24)$$

where ξ_L^R is the noise term. The variance of ξ_L^R is $\sigma_\xi^2 = 4\mathcal{N}_0\mathcal{E}_p N_f^2/(N_f+2)^2 \sum_{l=1}^{L_c}\sum_{n=1}^{N_f-1} |H_l(n-1)|^2$, with $\mathcal{N}_0/2$ being the variance of the time-domain sampled noise at the correlator output.

As in the complex-carrier case, one would expect a simpler decoder similar to (22) to hold also for the real-carrier case. This, however, is not straightforward, and the derivations we used for the complex case does not carry over. Intuitively, the low-complexity decoder in (22) relies on the fact that $H_l(0) \approx H_l(N_f-1)$. The counterpart condition for the real-carrier case would be $H_l(0) \approx H_l(N_f/2)$, which is evidently not true. Nevertheless, we proved in the Appendix that the following low-complexity decoder can be employed for the real-carrier low-rate setup:

$$u_L^R = \sum_{l=1}^{L_c} \sum_{n=0}^{N_f-1} |y^R(l;n)|^2 \cos\left(\frac{2\pi n}{N_f}\right). \quad (25)$$

The receiver structure is illustrated in Fig. 2. Similar to the complex case, the differential decoding can be performed by correlating $\{|y^R(l;n)|^2\}_{n=0}^{N_f-1}$ with the real carrier $\{\cos(2\pi n/N_f)\}_{n=0}^{N_f-1}$ on each correlator branch l, and then summing up all the L_c correlation results.

Remark 2: At low data rate, our MCD-UWB enjoys a simple receiver reminiscent of the FSR-UWB in [6]. However, FSR-UWB entails an inherent energy loss, simply because half of the energy per symbol is allocated to the reference tone. On the other hand, only a single reference tone (or even none) is employed in MCD-UWB, which consumes $1/N_f$ (or $2/(N_f+2)$ in the real carrier case) of the energy per symbol. In UWB systems with large N_f values, this implies considerable efficiency improvement.

C. Variable-Rate MCD-UWB

So far, we have seen that our MCD-UWB allows for both high-rate transmissions with (N_f-1) symbols per block, and low-rate transmissions with a low-complexity receiver. In fact, the MCD-UWB framework also enables transmissions with variable data rates to facilitate a desirable rate-performance tradeoff.

1) Complex Carriers: At the transmitter, with $N_s < N_f$ symbols being encoded in one block, the entries of the carrier modulating vector $\boldsymbol{d}^C$ can be differentially constructed group by group as follows:

$$d^C(n)=\begin{cases}1, & n=0\\ d^C(n-1)s(1), & n\in[1,\ldots,p^C(1)]\\ \vdots & \\ d^C(n-1)s(j), & n\in[p^C(j-1)+1,\ldots,p^C(j)]\\ \vdots & \\ d^C(n-1)s(N_s), & n\in[p^C(N_s-1)+1,\ldots,p^C(N_s)]\end{cases} \tag{26}$$

where $p^C(j)=\sum_{i=1}^{j} n_s(i), j\in[1,\ldots,N_s]$, $p^C(N_s)=N_f-1$, and $\{s(j)\}_{j=1}^{N_s}$ are the N_s information symbols each encoded on a group of $n_s(j)$ carriers. As with the high-rate case, the first carrier is used as the unmodulated reference [cf. (9) and (26)]. However, we will next show that it is possible to avoid the reference carrier, as in the low-rate case.

The decoding procedure for variable-rate MCD-UWB is similar to that of the high-rate case, except that the decision statistic of each symbol now relies on a group of carriers instead of a single carrier. To effectively collect energy, for each symbol $s(j)$, we sum up the decoding results from all L_c correlators and its corresponding $n_s(j)$ carriers. Using (14), the decision statistic for the jth information symbol is

$$u_V^C(j)=\sum_{n=p^C(j)-n_s(j)+1}^{p^C(j)}[\boldsymbol{U}^C]_{n,n},\quad j=[1,\ldots,N_s]. \tag{27}$$

With $H(n)\approx H(n+1)$, $n\in[0,\ldots,N_f-1]$, the noise-free part of $u_V^C(j)$ can be explicitly expressed as

$$u_V^C(j)\approx\sum_{n=p^C(j)-n_s(j)+1}^{p^C(j)}\sum_{l=1}^{L_c}\mathcal{E}_p|H_l(n)|^2s(j)\quad j=[1,\ldots,N_s]. \tag{28}$$

Recall that, as a manifestation of digital multicarrier modulation, we have also $H(0)\approx H(N_f-1)$. Similar to the low-rate case, this feature can be exploited to eliminate the need for any reference carrier by letting $d^C(N_f-1)s(N_s)=d^C(0)$. Together with $d^C(0)=1$ in (26), this condition implies $\prod_{j=1}^{N_s}s(j)^{n_s(j)}=1$. Considering the independence among $\{s(j)\}_{j=1}^{N_s}$, we have equivalently $s(j)^{n_s(j)}=1, j\in[1,\ldots,N_s]$. Therefore, as long as the modulation size of $s(j)$ is an integer factor of $n_s(j)$, our differential demodulation can be carried out between all adjacent pairs of digital carriers without any reference tone, and the noise free part of the decision static for $s(N_s)$ can be modified into $\sum_{n=p^C(N_s-1)+1}^{N_f-1}|H_l(n)|^2s(N_s)+|H_l(0)|^2s(N_s)$.

2) Real Carriers: In the variable-rate case, the entries of the carrier modulating vector $\boldsymbol{d}^R$ can be constructed group by group as follows:

$$d^R(n)=\begin{cases}1, & n=0\\ d^R(n-1)b(1), & n\in[1,\ldots,p^R(1)]\\ \vdots & \\ d^R(n-1)b(j), & n\in[p^R(j-1)+1,\ldots,p^R(j)]\\ \vdots & \\ d^R(n-1)b(N_b), & n\in[p^R(N_b-1)+1,\ldots,p^R(N_b)]\end{cases} \tag{29}$$

where $p^R(j)=\sum_{i=1}^{j}n_b(i), j\in[1,\ldots,N_b]$, $p^R(N_b)=N_f/2$ and $\{b(j)\}_{j=1}^{N_b}$ are N_b information bits each of which is encoded on a group of $n_b(j)$ carriers.

Similar to the reception in variable-rate case of complex carriers, to effectively collect energy, for each bit, we sum up the decoding results from all correlators and all corresponding carriers. Using the definition of $\boldsymbol{U}^R=\sum_{l=1}^{L_c}\boldsymbol{v}^R(l)(\boldsymbol{v}^R(l))^T\boldsymbol{J}^R$ of (17), the decision static for the jth information bit can be expressed as

$$u_V^R(j)=\sum_{n=p^R(j)-n_b(j)+1}^{p^R(j)}[\boldsymbol{U}^R]_{n,n},\quad j=[1,\ldots,N_b]. \tag{30}$$

For $\Re\{H_l(n)\}=\Re\{H_l(n+1)\}$, $n\in[0,\ldots,N_f/2]$, the noise-free parts of the decision statistics are

$$u_V^R(j)\approx\frac{4\mathcal{E}_pN_f^2}{(N_f+2)^2}\sum_{n=p^R(j)-n_b(j)+1}^{p^R(j)}\sum_{l=1}^{L_c}\Re\{H_l(n)\}^2\cdot b(j),\quad j=[1,\ldots,N_b]. \tag{31}$$

However, unlike the complex-carrier case where $H(0)\approx H(N_f-1)$, for real-carrier MCD-UWB, it does not hold that $H(0)\approx H(N_f/2)$. Therefore, the first and last carriers cannot be differentially related with respect to the information symbol $b(N_b)$, and a reference tone should always be used.

Though both the complex and the real MCD-UWB can enable variable-rate communications, it is worth noting that the maximum number of carriers in the complex MCD-UWB (N_f) nearly doubles that of the real MCD-UWB $(N_f/2+1)$. Therefore, for variable-rate MCD-UWB, when the data rate is fixed, the complex-carrier case can use more carriers per symbol. We will see later that the number of carriers per symbol is closely related to the diversity gain and the demodulation performance. Another difference between the real and complex MCD-UWB is that, the complex case requires the channel to be invariant

in $2T_s$, but the real case only needs the channel to be invariant in T_s.

D. MCD-UWB Versus FSR-UWB

So far, we have established the differential coding and decoding of our MCD-UWB for both high-rate and low-rate implementations. As the FSR-UWB, our approach also avoids analog delay lines. However, the energy loss of the FSR-UWB is considerably reduced in our MCD-UWB especially for typically large N_f values. For the high-rate case, both MD-FSR-UWB and MCD-UWB use a single carrier as the reference tone, and multiple carriers for information symbols. Unlike the MD-FSR-UWB, however, the number of information-conveying carriers of MCD-UWB is not limited by the coherence bandwidth. Furthermore, thanks to the digital operation, our MCD-UWB does not induce any bandwidth expansion. In addition, MCD-UWB allows for (possibly severe) IFI that is inevitable in high-rate transmissions.

V. Performance Analysis

So far, we have introduced the multicarrier differential UWB schemes which enable the variable data rates. In addition, at low data rate, the demodulation can be further simplified. In this section, we analyze the error performance of MCD-UWB. Specifically, we will study the effects of the variable data rates on the BER performance for the cases of both complex and real carriers.

A. Complex MCD-UWB

In the cases of high, low, and variable rates, the major difference lies in the different numbers of carriers each symbol occupies. Without loss of generality, let us now focus on the complex multicarrier case, and consider the pairwise error probability (PEP) of erroneously decoding s as $s' \neq s$ with a maximum likelihood (ML) detector, assuming that s is differentially encoded on the first n_s carriers. The PEP can be upper bounded at high signal-to-noise ratio (SNR) using the Chernoff bound[2]

$$P(s \to s') \leq \exp\left(\frac{-d^2(u^C, u^{C'})}{4\sigma_\xi^2}\right) \tag{32}$$

where σ_ξ^2 is the variance of the complex noise, and $u^C(u^{C'})$ is the noise-free part of the demodulation result corresponding to $s(s')$, and $d(u^C, u^{C'})$ is the Euclidean distance between u^C and $u^{C'}$.

Using $u^C \approx \mathcal{E}_p \sum_{l=1}^{L_c} \sum_{n=0}^{n_s-1} |H_l(n)|^2 s(n)$ [cf. (28)], we have

$$d^2(u^C, u^{C'}) = \left(\mathcal{E}_p \sum_{l=1}^{L_c} \sum_{n=0}^{n_s-1} |H_l(n)|^2\right)^2 |\epsilon|^2 \tag{33}$$

[2]Though the noise-by-noise terms in our decision statistics are not strictly Gaussian distributed, they are approximately so under the Central Limit Theorem. In addition, these noise-by-noise terms are negligible under the high SNR scenario of interest here.

where $\epsilon := s - s'$. At high SNR, (32) can be re-expressed as

$$\begin{aligned} P(s \to s') &\leq \exp\left(-\frac{\mathcal{E}_p|\epsilon|^2}{8\mathcal{N}_0} \sum_{l=1}^{L_c} \sum_{n=0}^{n_s-1} |H_l(n)|^2\right) \\ &= \exp\left(-\frac{N_f \mathcal{E}_p |\epsilon|^2}{8\mathcal{N}_0} \sum_{l=1}^{L_c} \sum_{n=0}^{n_s-1} \boldsymbol{\beta}_c(l)^T \boldsymbol{\Theta}_l^C \boldsymbol{\beta}_c(l)\right) \end{aligned} \tag{34}$$

where $\boldsymbol{\beta}_c(l) = [\beta_c(l;0), \ldots, \beta_c(l;M_l)]^T$ and $\boldsymbol{\Theta}_l^C := \boldsymbol{F}_{0:n_s-1,0:M_l}^{\mathcal{H}} \boldsymbol{F}_{0:n_s-1,0:M_l}$, with $\boldsymbol{F}_{0:n_s-1,0:M_l}$ denoting the matrix consisting of the first n_s rows and the first (M_l+1) columns of $\boldsymbol{F}$. With $\beta_c(l;m)$ being zero-mean, i.i.d. Gaussian with variance $\mathcal{B} = E\{\beta_c^2(l;m)\}$, the average PEP can be upper bounded by (see, e.g., [18], [20])

$$\bar{P}(s \to s') \leq \prod_{l=1}^{L_c} \prod_{m=0}^{M_l} \left[1 + \frac{N_f \mathcal{E}_p \mathcal{B}|\epsilon|^2}{4\mathcal{N}_0} \lambda_l^C(m)\right]^{(-1/2)} \tag{35}$$

where $\{\lambda_l^C(m)\}_{m=0}^{M_l}$ are the eigenvalues of $\boldsymbol{\Theta}_l^C$ in the non-increasing order. Letting r_l^C denote the rank of $\boldsymbol{\Theta}_l^C$, we have $\lambda_l^C(m) \neq 0$ if and only if $m \in [0, \ldots, r_l^C - 1]$. The maximum rank of $\boldsymbol{\Theta}_l^C$ is $r_l^C = \min\{n_s, M_l + 1\}$. Therefore, at high SNR ($\mathcal{E}_p/\mathcal{N}_0 \gg 1$), (35) becomes

$$\bar{P}(s \to s') \leq \left(\frac{N_f \mathcal{E}_p \mathcal{B}|\epsilon|^2}{4\mathcal{N}_0}\right)^{-\sum_{l=1}^{L_c} r_l^C/2} \prod_{l=1}^{L_c} \prod_{m=0}^{r_l^C-1} \lambda_l^C(m)^{(-1/2)}. \tag{36}$$

The average PEP can usually be expressed with the following general form

$$\bar{P}(\epsilon \neq 0) \leq \left(\frac{\mathcal{E}_p}{\mathcal{N}_0} G_{c,\epsilon}\right)^{-G_d} \tag{37}$$

where

$$\begin{aligned} G_d &= \frac{1}{2} \sum_{l=1}^{L_c} \min\{M_l + 1, n_s\} \\ G_{c,\epsilon} &= \frac{N_f \mathcal{B}|\epsilon|^2}{4} \left(\prod_{l=1}^{L_c} \lambda_l^C\right)^{(1/2G_d)}. \end{aligned} \tag{38}$$

Evidently G_d determines the PEP slope as a function of log-$\mathcal{E}_p/\mathcal{N}_0$ and is the so-termed diversity gain, and $G_{c,\epsilon}$ denotes the coding gain which determines the horizonal shift. Notice that G_d is independent of the specific error ϵ, whereas $G_{c,\epsilon}$ is ϵ dependent. To account for all possible pairwise errors, we define the coding gain as $G_c := \min_{\epsilon \neq 0}\{G_{c,\epsilon}\}$.

We are now ready to specify the diversity and coding gains at each data rate level. For the high-rate case, where the carrier number per symbol is $n_s = 1$, the rank of $\boldsymbol{\Theta}_l^C$ is one, and, therefore, the diversity gain is $G_d = L_c/2$. For the variable-rate case, the diversity gain analysis is the same as the preceding analysis under the general condition, i.e., $G_d = 0.5 \sum_{l=1}^{L_c} \min\{M_l + 1, n_s(j)\}, \forall\, j \in [1, \ldots, N_s]$, for the jth transmitted symbol. For the low-rate case where only one information symbol is transmitted, we obtain that $G_d = 0.5 \sum_{l=1}^{L_c} (M_l + 1)$. Comparing the diversity gains at different data rate levels, we deduce that the

more carriers are used to carry one symbol, the higher diversity gain can be achieved. This, however, is at the price of reduced data rate. Therefore, there is a tradeoff between the data rate and the error performance.

Remark 3: Equation (38) shows that the diversity order G_d depends on both the number of carriers per symbol n_s and the channel orders $\{M_l\}_{l=1}^{L_c}$, which capture the severity of IFI. In the general case where IFI is present ($M_l \neq 0$), the diversity gain is $G_d = 0.5\sum_{l=1}^{L_c}(M_l+1)$, as long as $n_s \geq M_l+1$, $\forall\, l$. On the other hand, one may opt to avoid IFI in the first place, by choosing T_f to be large enough. In this case, we have $M_l = 0$, $\forall\, l$. It follows that the diversity order is $G_d = L_c/2$ regardless of n_s. Therefore, with fixed number of correlators L_c, the IFI actually works to our advantage by enabling a greater G_d.

Remark 4: To reduce the peak-to-average power ratio (PAPR) of the transmitted waveform, we can also use $N_c < N_f$ carriers. For example, for the low-rate case, the diversity gain is $G_d = 0.5\sum_{l=1}^{L_c}\min\{M_l+1, N_c\}$. By using less carriers, the PAPR effects can be suppressed, and the diversity gain will decrease consequently. Therefore, there is also a tradeoff between the PAPR suppression and the symbol error rate performance. Notice that, as long as N_c is greater than the maximum order of the equivalent channel, the maximum diversity gain $0.5\sum_{l=1}^{L_c}(M_l+1)$ can always be achieved.

B. Real MCD-UWB

Similar to the complex-carrier MCD-UWB, for the case of real carriers, we first consider the general case when one bit b is conveyed by n_b carriers. The average PEP can be upper bounded by

$$\bar{P}(b\to b') \leq \prod_{l=1}^{L_c}\prod_{m=0}^{M_l}\left[1+\frac{2N_f^3\mathcal{E}_p\mathcal{B}\epsilon_b^2}{\mathcal{N}_0(N_f+2)^2}\lambda_l^R(m)\right]^{-(1/2)} \tag{39}$$

where $\epsilon_b = (b-b')$ and $\{\lambda_l^R(m)\}_{m=0}^{M_l}$ are the eigenvalues of $\boldsymbol{\Theta}_l^R := \Re\{\boldsymbol{F}_{0:n_b-1,0:M_l}\}^T\Re\{\boldsymbol{F}_{0:n_b-1,0:M_l}\}$ in the nonincreasing order. The maximum rank of $\boldsymbol{\Theta}_l^R$ is $r_l^R = \min\{M_l+1, n_b\}$. Therefore, the maximum achievable diversity order is $0.5\sum_{l=1}^{L_c}\min\{M_l+1, n_b\}$. Specifically, for the high-rate case, where every bit is riding on a single carrier, the diversity gain is $G_d = L_c/2$. For the variable-rate case, we have $G_d = 0.5\sum_{l=1}^{L_c}\min\{M_l+1, n_b(j)\}$ for the jth bit, $\forall\, j \in [1,\ldots,N_b]$. Similarly, for low-rate real-carrier MCD-UWB, where all $N_f/2$ carriers are modulated by a single bit, we have $G_d = 0.5\sum_{l=1}^{L_c}\min\{M_l+1, N_f/2\}$. Similar to the complex MCD-UWB, using variable number of carriers to carry one bit also allows for a flexible tradeoff between the data rate and the diversity order.

As with the complex MCD-UWB, Remarks 3 and 4 also hold in the real carrier case. In particular, consider MCD-UWB with two real carriers ($N_c = 2$), which can be regarded as the digital version of the FSR-UWB scheme. The noise-free part of its decision statistic is [cf. (42)]

$$u_L^R \approx \frac{N_f\mathcal{E}_p}{2\sqrt{2}}\sum_{l=1}^{L_c}\left(|H_l(0)|^2+|H_l(N_f-1)|^2\right)b. \tag{40}$$

Accordingly, the maximum diversity gain can be obtained as $0.5\sum_{l=1}^{L_c}\min\{M_l+1, 2\}$. Clearly, when more than two frames are involved in the IFI, i.e., $M_l > 1$, the MCD-UWB with $N_c > 2$ carriers carrying each bit can provide a greater diversity gain.

Remark 5: As mentioned before, the maximum number of carriers in the complex MCD-UWB (N_f) is greater than that of the real MCD-UWB ($N_f/2+1$). Therefore, for a fixed data rate, the complex case can use more carriers per symbol. According to the preceding diversity analysis, this implies a better error performance with a larger diversity gain G_d. On the other hand, the complex MCD-UWB enables a higher data rate than the real MCD-UWB when G_d is fixed.

VI. Simulations

In our simulations, the UWB pulse $p(t)$ is the second derivative of the Gaussian pulse with $T_p \approx 1$ ns. Each T_s consists of $N_f = 32$ frames. Simulations are performed using the Saleh–Valenzuela channel model with parameters $(1/\Lambda, 1/\lambda, \Gamma, \gamma) = (2, 0.5, 30, 5)$ ns [15]. The maximum delay spread of the multipath channel is about 90 ns. The real- and complex-carrier cases adopt BPSK and QPSK modulations, respectively. For both cases, we use $L_c = 6$ correlators with $\tau_c(l) = (l-1)$ ns, $\forall\, l \in [1,\ldots,L_c]$.

In the first test scenario, we compare the bit-error rate (BER) performance with and without IFI. As mentioned in the preceding section, one can either allow for IFI and remove the IBI via CP, or avoid IFI by choosing a large T_f. For the former case, we let $T_f = 24$ ns and employ CP of length 4 (frames). For the latter case, we let $T_f = 96$ ns.

Figs. 3 and 4 show the comparisons between the CP-assisted and IFI-free cases for both complex and real MCD-UWB, respectively. In both figures, the BER curves are nearly parallel at high $\mathcal{E}_p/\mathcal{N}_0$ for the IFI-free cases. This indicates that the diversity gain does not change when the number of carriers per symbol increases. However, with the use of CP, the slope of the BER curve drops as the number of carriers per symbol increases. These confirm that the CP-assisted schemes outperform the IFI-free ones in terms of the diversity gain, as predicted by the performance analysis in the preceding section. It is also worth noting that the CP-based scheme provides 3.66 times the data rate of the IFI-free case. In the following, we will set $T_f = 24$ ns.

To validate the effects of the number of carriers per symbol on the error performance, we plot in Figs. 5 and 6 the BER curves for the low-rate complex and real MCD-UWB with various N_c values. In all cases, only one symbol is transmitted per block of duration T_s. First, we observe that the complex- and real-carrier schemes have similar performances as predicted by the analysis in the preceding section. In both figures, the curves corresponding to larger N_c values exhibit better BER performance. This is in part due to their greater diversity gains which give rise to steeper slopes of the BER curves, as indicated in our performance analysis. Another reason for the performance improvement with increasing N_c is the improved energy efficiency. In particular, notice that the case with $N_c = 2$ can be regarded as the digital version of FSR-UWB, in the sense that half of the energy is used by the reference tone. This further illustrates that

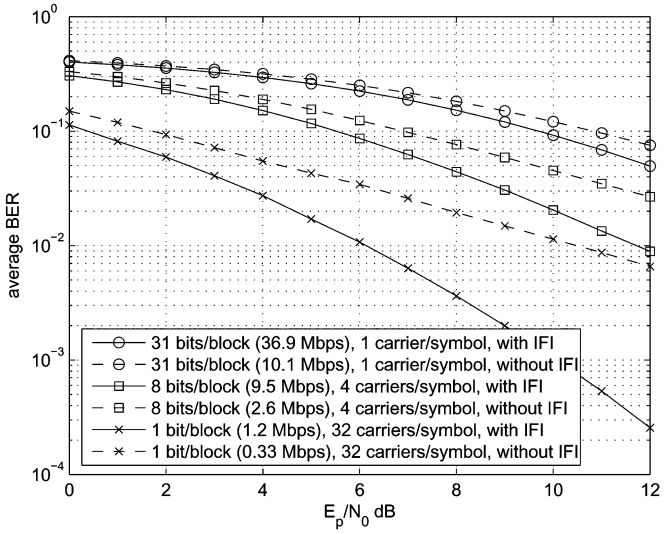

Fig. 3. Complex MCD-UWB with various data rates, and in the presence and absence of IFI.

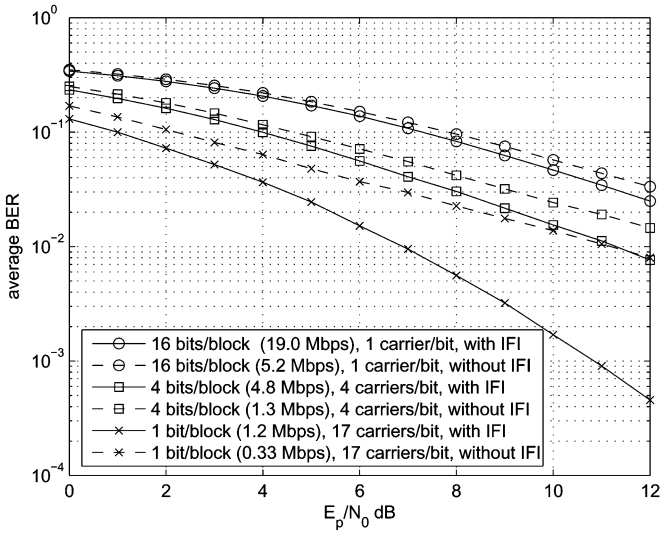

Fig. 4. Real MCD-UWB with various data rates, and in the presence and absence of IFI.

MCD-UWB can be more energy efficient than the FSR-UWB by enabling a larger N_c.

As mentioned before, the maximum number of the complex carriers is nearly twice that of the real carriers. Therefore, with a fixed data rate, complex MCD-UWB can allocate more carriers to each symbol. Indeed, Fig. 7 shows that, with a fixed data rate of 2 bits/block, the complex case outperforms the real case by 3 dB at BER $= 10^{-4}$. With both cases using eight carriers per symbol, the complex and real MCD-UWB schemes achieve the same diversity order and nearly identical performance, as shown in Fig. 7. However, the complex MCD-UWB provides a data rate of 4 bits per block, which doubles that of the real MCD-UWB.

In Fig. 8, we also compare the performance of the MD-FSR-UWB with our variable-rate MCD-UWB. For MD-FSR-UWB, the one-sided noise bandwidth is 4 GHz. The rms delay spread of the simulation channel is $\sigma_{\rm rms} \approx 9$ ns, which gives rise to a coherence bandwidth of about 22 MHz.

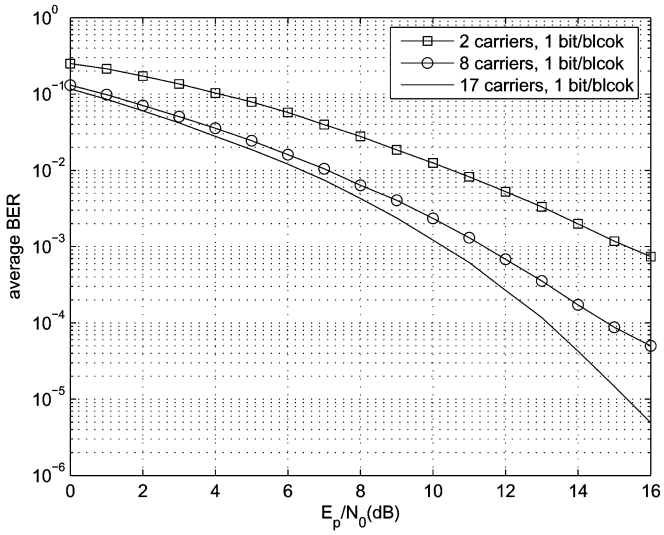

Fig. 5. Low-rate complex MCD-UWB.

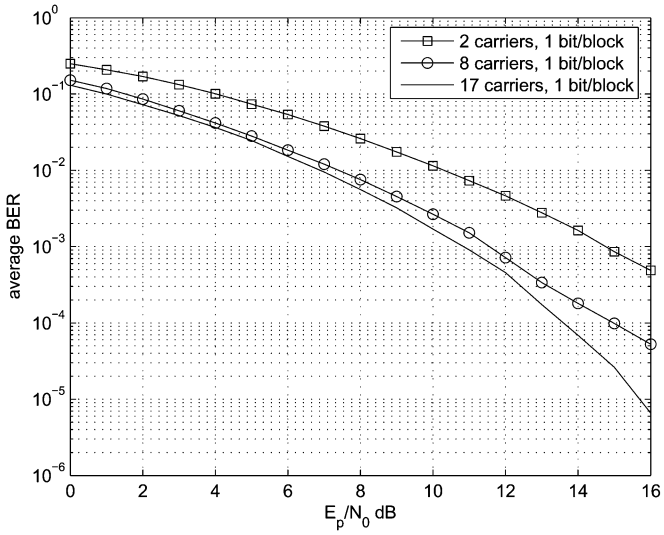

Fig. 6. Low-rate real MCD-UWB.

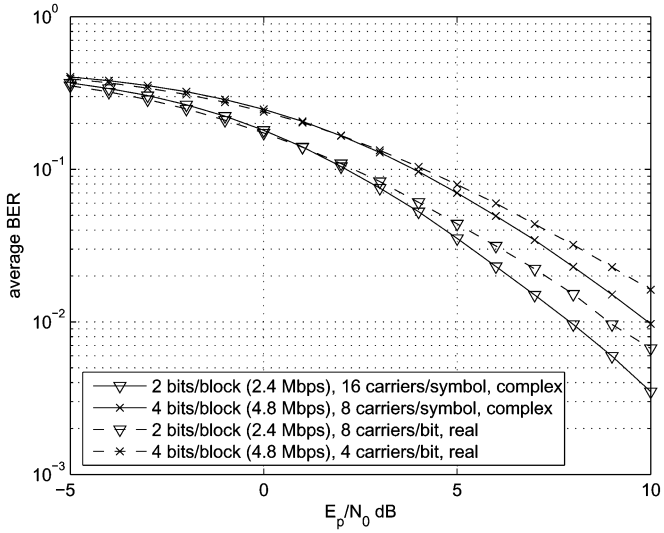

Fig. 7. MCD-UWB with various data rates.

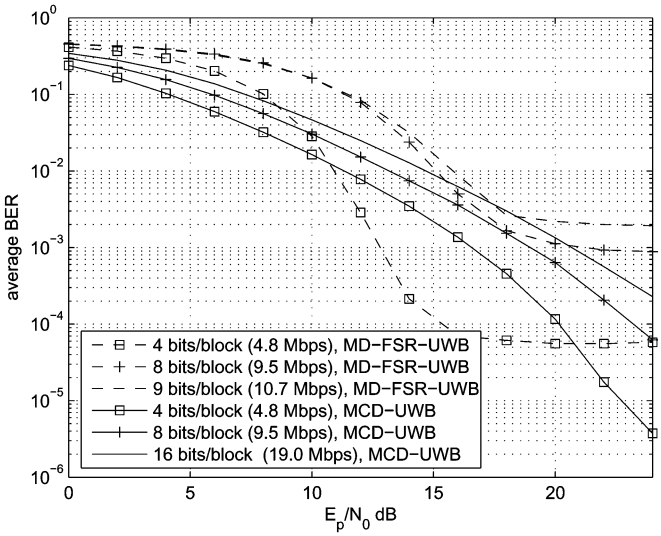

Fig. 8. MCD-UWB versus MD-FSR-UWB at various data rates.

With the carrier spacing of $1/(N_fT_f) \approx 1.3$ MHz, the MD-FSR-UWB can transmit a maximum of 9 bits per block. With 17 real carriers, our MCD-UWB can transmit up to 16 bits per block. In addition, notice that the 9 bits per block of MD-FSR-UWB is achieved at the price of bandwidth expansion, where as MCD-UWB does not entail any bandwidth expansion. Fig. 8 shows that the BER curves for the MD-FSR-UWB are flat at low SNR, have steep slopes at moderate SNR, and flatten again at high SNR. The low-SNR flatness may be induced by the dominant double-noise term. The steep slope at moderate SNR reveals the considerable diversity order achieved by the MD-FSR-UWB. At high SNR values where the noise can be neglected, the BER performance of MD-FSR-UWB is limited by the discrepancy between the channel responses at the reference tone and the date-conveying tones. This limitation results in the flatness at high SNR. Since the higher data rate in MD-FSR-UWB is achieved at the price of increased frequency separation among the reference and data-conveying tones, the error floor level increases with the increasing data rate, as shown in Fig. 8. The MCD-UWB BER curves exhibit a more consistent performance, simply because the spacing between the reference and data tones remains invariant at any data rate.

Comparing the BER curves in Fig. 8, we also notice that, at relatively low data rate (4 bits per block), MCD-UWB outperforms MD-FSR-UWB at low and high SNR, while the latter outperforms the former at moderate SNR. At a higher data rate of 8 bits per block, the MCD-UWB outperforms the MD-FSR-UWB at all SNR values. At their respective maximum rates of 16 and 9 bits/block, our MCD-UWB still outperforms the MD-FSR-UWB at almost all SNRs while providing twice the data rate. It is worth noting that only 6 correlators are used for the MCD-UWB, which collects energy over only $6/24 = 25\%$ of each frame duration T_f. The error performance of MCD-UWB is expected to be further enhanced by increasing the number of correlators.

VII. Conclusion

In this paper, we have introduced the digital multicarrier differential signaling schemes for UWB communications. Our frequency-domain differential approach is inspired by the FSR-UWB, and can avoid the challenging UWB channel estimation without imposing the analog delay elements. However, with the employment of multiple digital carriers, our MCD-UWB outperforms FSR-UWB by avoiding the bandwidth expansion as well as the energy loss. Compared to the high-rate version of FSR-UWB (a.k.a. MD-FSR-UWB), our approach allows for higher data rates without being constrained by the channel coherence bandwidth, and without degrading the demodulation performance, by maintaining the minimum spacing between the data tone and its corresponding "reference" tone. Our MCD-UWB enables diversity combining in a differential manner and ensures effective collection of the multipath diversity, even in the presence of severe IFI and ISI. The proposed multicarrier modulation can be realized with standard FFT and DCT circuits, both operating at the frame-rate.

Appendix

To avoid terms containing $H_l(0)H_l(N_f/2)$ to appear in the decision statistic, we will resort to the $N_f \times N_f$ shifting matrix $\boldsymbol{J}$. It appears that we can use $\sum_{l=1}^{L_c}(\boldsymbol{y}^R)^T(l)\bar{\boldsymbol{G}}\boldsymbol{J}\bar{\boldsymbol{G}}^T\boldsymbol{y}^R(l)$ as the decision statistic like the complex-carrier case [cf. (20)], where the $N_f \times N_f$ matrix $\bar{\boldsymbol{G}} = [\boldsymbol{g}_0, \ldots, \boldsymbol{g}_{N_f/2}, \boldsymbol{0}, \ldots, \boldsymbol{0}]$ is constructed by concatenating $\boldsymbol{G}$ with $(N_f/2-1)$ zero vectors of size N_f. However, unlike the complex case where $\boldsymbol{F}^{\mathcal{H}}\boldsymbol{J}\boldsymbol{F}$ is a diagonal matrix [cf. (22)], $\bar{\boldsymbol{G}}\boldsymbol{J}\bar{\boldsymbol{G}}^T$ does not have a form which can lead to the simple receiver structure as the complex-carrier case.

For these reasons, we use FFT and IFFT operations with the shifting matrix $\boldsymbol{J}$ to enable a simple receiver for the real-carrier low-rate case. Denoting the FFT of $\boldsymbol{y}^R(l)$ as $\bar{\boldsymbol{v}}^R(l) := \boldsymbol{F}\boldsymbol{y}^R(l)$, we have

$$\bar{u}_L^R = \sum_{l=1}^{L_c}(\bar{\boldsymbol{v}}^R(l))^{\mathcal{H}}\boldsymbol{J}\bar{\boldsymbol{v}}^R(l) = \sum_{l=1}^{L_c}(\boldsymbol{y}^R(l))^{\mathcal{H}}\boldsymbol{F}^{\mathcal{H}}\boldsymbol{J}\boldsymbol{F}\boldsymbol{y}^R(l)$$
$$\approx \sum_{l=1}^{L_c}\mathcal{E}_p(\boldsymbol{d}^R)^T\boldsymbol{G}^T\boldsymbol{F}^{\mathcal{H}}\boldsymbol{J}|\boldsymbol{D}_H(l)|^2\boldsymbol{F}\boldsymbol{G}\boldsymbol{d}^R + \bar{\xi}_L^R \qquad (41)$$

where the approximation comes from $H(n) \approx H(n+1)$, $n \in [0, \ldots, N_f-1]$, and $\bar{\xi}_L^R$ is the noise term.

Let $\boldsymbol{J}_H(l)$ denote the real part of $\boldsymbol{G}^T\boldsymbol{F}^{\mathcal{H}}\boldsymbol{J}|\boldsymbol{D}_H(l)|^2\boldsymbol{F}\boldsymbol{G}$ which is an $(N_f/2+1)\times(N_f/2+1)$ tridiagonal matrix with the main diagonal being zero, and vectors

$$N_f/(N_f+2)[\sqrt{2}|H_l(N_f-1)|^2, |H_l(N_f-2)|^2, \ldots, |H_l(N_f/2+1)|^2, \sqrt{2}|H_l(N_f/2)|^2]$$

and

$$N_f/(N_f+2)\left[\sqrt{2}|H_l(0)|^2, |H_l(1)|^2, \ldots, |H_l(N_f/2-2)|^2, \sqrt{2}|H_l(N_f/2-1)|^2\right]$$

$$
\begin{aligned}
u_L^R &= \Re\left(\bar{u}_L^R\right) \approx \mathcal{E}_p \sum_{l=1}^{L_c} \boldsymbol{d}^T \boldsymbol{J}_H(l)\boldsymbol{d} + \xi_L^R \\
&= \frac{\sqrt{2}N_f}{N_f+2}\mathcal{E}_p \sum_{l=1}^{L_c}\left[|H_l(0)|^2 + \left|H_l\left(\frac{N_f}{2}\right)\right|^2 + |H_l(N_f-1)|^2 + \left|H_l\left(\frac{N_f-1}{2}\right)\right|^2\right] b \\
&\quad + \frac{N_f}{N_f+2}\mathcal{E}_p \sum_{l=1}^{L_c}\sum_{n=1}^{(N_f/2-2)}\left[|H_l(n)|^2 + \left|H_l\left(n+\frac{N_f}{2}\right)\right|^2\right] b + \xi_L^R,
\end{aligned} \tag{42}
$$

sitting on the subdiagonals. Then, the decision statistic of b can be obtained as the real part of $\bar{u}_L^R$, as shown in (42) at the top of the page, where ξ_L^R is the real part of $\bar{\xi}_L^R$. The noise-free part of u_L^R contains the information bit b.

As with the case of complex carriers, the receiver structure for real carriers can be further simplified. By replacing $\boldsymbol{F}^{\mathcal{H}}\boldsymbol{J}\boldsymbol{F}$ with $\boldsymbol{D}_J$ in (41), u_L^R can be re-expressed by

$$
u_L^R = \sum_{l=1}^{L_c}\sum_{n=0}^{N_f-1} |y^R(l;n)|^2 \cos\left(\frac{2\pi n}{N_f}\right).
$$

ACKNOWLEDGMENT

The authors would like to thank Dr. D. L. Goeckel for his comments and suggestions that helped improve the quality of this paper.

REFERENCES

[1] Y. Chao and R. A. Scholtz, "Ultra-wideband transmitted reference systems," *IEEE Trans. Veh. Technol.*, vol. 54, no. 9, pp. 1556–1569, Sep. 2005.

[2] D. Gerakoulis and P. Salmi, "An interference suppressing OFDM system for ultra wide bandwidth radio channels," in *Proc. IEEE Conf. Ultra-Wideband Syst. Technol.*, Baltimore, MD, May 2002, pp. 259–264.

[3] S. S. Ghassemzadeh, R. Jana, V. Tarokh, C. W. Rice, and W. Turin, "A statistical path loss model for in-home UWB channels," in *Proc. IEEE Conf. Ultra-Wideband Syst. Technol.*, Baltimore, MD, May 2002, pp. 59–64.

[4] W. M. Gifford and M. Z. Win, in *Proc. Asilomar Conf. Signals, Syst. Comput.*, Pacific Grove, CA, Nov. 2004, pp. 1526–1531.

[5] D. L. Goeckel and Q. Zhang, in *Proc. MILCOM Conf.*, Atlantic City, NJ, Oct. 2005, pp. 3029–3035.

[6] D. L. Goeckel and Q. Zhang, "Slightly frequency-shifted reference ultra-wideband (UWB) radio," *IEEE Trans. Commun.*, vol. 55, no. 3, pp. 508–519, Mar. 2007.

[7] N. He and C. Tepedelenlioglu, "Adaptive synchronization for non-coherent UWB receivers," in *Proc. Int. Conf. Acoust., Speech, Signal Process.*, Montreal, CA, May 2004, pp. 517–520.

[8] N. He and C. Tepedelenlioglu, "Performance analysis of non-coherent UWB receivers at different synchronization levels," in *Proc. Global Telecommun. Conf.*, Dallas, TX, Nov.–Dec. 2004, pp. 3517–3521.

[9] M. Ho, V. Somayazulu, J. Foerster, and S. Roy, "A differential detector for an ultra-wideband communications system," in *Proc. Veh. Technol. Conf.*, Birmingham, AL, May 2002, pp. 1896–1900.

[10] R. T. Hoctor and H. W. Tomlinson, "An overview of delay-hoped, transmitted-reference RF communications," *G.E. Research and Development Center, Technical Information Series*, pp. 1–29, Jan. 2002.

[11] J. Keignart and N. Daniele, "Subnanosecond UWB channel sounding in frequency and temporal domain," in *Proc. IEEE Conf. Ultra-Wideband Syst. Technol.*, Baltimore, MD, May 2002, pp. 25–30.

[12] J. Proakis, *Digital Communications*, 4th ed. New York: McGraw-Hill, 2001.

[13] T. S. Rappaport, *Wireless Communications: Principles and Practice*, 2nd ed. Englewood Cliffs, NJ: Prentice-Hall, 2002.

[14] C. Rushforth, "Transmitted-reference techniques for random or unknown channels," *IEEE Trans. Inf. Theory*, vol. IT-10, no. 1, pp. 39–42, Jan. 1964.

[15] A. A. M. Saleh and R. A. Valenzuela, "A statistical model for indoor multipath propagation," *IEEE J. Sel. Areas Commun.*, vol. SAC-5, no. 2, pp. 128–137, Feb. 1987.

[16] Z. Wang, "Multi-carrier ultra-wideband multiple-access with good resilience against multiuser interference," presented at the Conf. Inf. Sci. Syst., Baltimore, MD, Mar. 2003.

[17] Z. Wang and G. B. Giannakis, "Wireless multicarrier communications: Where Fourier meets Shannon," *IEEE Signal Process. Mag.*, vol. 47, no. 3, pp. 29–48, May 2000.

[18] Z. Wang and G. B. Giannakis, "Complex-field coding for OFDM over fading wireless channels," *IEEE Trans. Inf. Theory*, vol. 49, no. 3, pp. 707–720, Mar. 2003.

[19] M. Z. Win and R. A. Scholtz, "Ultra wide bandwidth time-hopping spread-spectrum impulse radio for wireless multiple access communications," *IEEE Trans. Commun.*, vol. 48, no. 4, pp. 679–691, Apr. 2000.

[20] L. Yang and G. B. Giannakis, "Digital-carrier multi-band user codes for baseband UWB multiple access," *J. Commun. Netw.*, vol. 5, no. 4, pp. 374–385, Dec. 2003.

[21] L. Yang and G. B. Giannakis, "Ultra-wideband communications: An idea whose time has come," *IEEE Signal Process. Mag.*, vol. 21, no. 6, pp. 26–54, Nov. 2004.

[22] L. Yang, G. B. Giannakis, and A. Swami, "Noncoherent ultra-wideband radios," presented at the MILCOM Conf., Monterey, CA, Oct.–Nov. 2004.

[23] Q. Zhang and D. L. Goeckel, "Multi-differential slightly frequency-shifted reference ultra-wideband (UWB) radio," presented at the Conf. Info. Sci. Syst., Princeton, NJ, Mar. 2006.

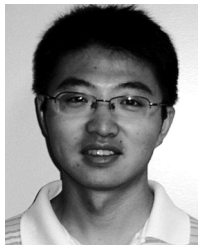

Huilin Xu received the B.Sc. and M.Sc. degrees, both in electrical engineering, from the University of Science and Technology of China (USTC), Hefei, China, in 2002 and 2005, respectively. He is currently pursuing the Ph.D. degree with the Department of Electrical and Computer Engineering, University of Florida, Gainesville.

His research interests are in the areas of wireless communications and related fields.

Liuqing Yang (S'02–M'04–SM'06) received the M.Sc. and Ph.D. degrees in electrical and computer engineering from the University of Minnesota, Minneapolis, in 2002 and 2004, respectively.

Since August 2004, she has been an Assistant Professor with the Department of Electrical and Computer Engineering, University of Florida, Gainesville.

Dr. Yang received the Best Dissertation Award in the Physical Sciences and Engineering from the University of Minnesota in 2005, and the Office of Naval Research Young Investigator Award in 2007.